Elsevier Editorial System(tm) for Remote Sensing of Environment
Manuscript Draft

Manuscript Number: RSE-D-18-00227R4

Title: New neural network cloud mask algorithm based on radiative transfer simulations

Article Type: Research Paper

Keywords: cloud mask; machine learning; radiative transfer modeling; cryosphere; snow and ice

Corresponding Author: Dr. Nan Chen,

Corresponding Author's Institution:

First Author: Nan Chen

Order of Authors: Nan Chen; Wei Li; Charles Gatebe; Tomonori Tanikawa; Masahiro Hori; Rigen Shimada; Teruo Aoki; Knut Stamnes

***Highlights (for review)**

Highlights:

- Machine learning based cloud mask algorithm
- Training dataset is generated by simulation data
- Validated by collocated CALIOP/MODIS data
- Consistent performance over different underlying surface types
- Easy to re-configure to be applicable to another sensor

New neural network cloud mask algorithm based on radiative transfer simulations

Nan Chen[1,*], Wei Li[1], Charles Gatebe[2], Tomonori Tanikawa[3], Masahiro Hori[4], Rigen Shimada[4], Teruo Aoki[5], Knut Stamnes[1]

Abstract

Cloud detection and screening constitute critically important first steps required to derive many satellite data products. Traditional threshold-based cloud mask algorithms require a complicated design process and fine tuning for each sensor, and they have difficulties over areas partially covered with snow/ice. Exploiting advances in machine learning techniques and radiative transfer modeling of coupled environmental systems, we have developed a new, threshold-free cloud mask algorithm based on a neural network classifier driven by extensive radiative transfer simulations. Statistical validation results obtained by using collocated CALIOP and MODIS data show that its performance is consistent over different ecosystems and significantly better than the MODIS Cloud Mask (MOD35 C6) during the winter seasons over snow-covered areas in the mid-latitudes. Simulations using a reduced number of satellite channels also show satisfactory results, indicating its flexibility to be configured for different sensors. Compared to threshold-based methods and previous machine-learning approaches, this new cloud mask (i) does not rely on thresholds, (ii) needs fewer satellite channels, (iii) has superior performance during winter seasons in mid-latitude areas, and (iv) can easily be applied to different sensors.

*Corresponding author
Email address: nchen@stevens.edu (Nan Chen)
[1]Department of Physics, Stevens Institute of Technology, Hoboken, New Jersey
[2]NASA GSFC, Greenbelt, MD, USA
[3]Meteorological Research Institute, Tsukuba, Japan
[4]Japan Aerospace Exploration Agency, Tsukuba, Japan
[5]Okayama University, Okayama, Japan

Keywords: , Cloud mask, machine learning, radiative transfer

2010 MSC: 00-01, 99-00

1. Introduction

1.1. Background

A reliable cloud mask is essential for satellite remote sensing of land, ocean, or cryospheric properties. Due to the significant impact of clouds on shortwave and longwave radiation, mis-identification of cloudy pixels as surface or vice versa can significantly affect the quality of any satellite remote sensing product. Traditionally, threshold-based tests have been employed in many cloud mask algorithms. Such algorithms include the Automated Cloud Cover Assessment (ACCA) algorithm (Irish et al., 2006) applied to the Landsat ETM+ sensor, the cloud tests applied in the MOD35 algorithm (Ackerman et al., 2010) for the moderate-resolution imaging spectroradiometer (MODIS) sensor and the Clouds from AVHRR (CLAVR) (Stowe et al., 1999) as well as its extension CLAVR-x algorithm. These algorithms typically use a combination of threshold tests, which employ a number of satellite channels located in the visible (VIS), near infrared (NIR), shortwave infrared (SWIR), and thermal infrared (TIR) wavelength ranges (e.g. MOD35 uses 19 bands – 10 reflectance bands and 9 thermal infrared bands) to detect clouds and snow/ice. The thresholds used in these tests are generally from 1) model simulations, 2) statistics of cloud/clear-sky scenes, and 3) expert experience. New algorithms, such as fmask (Zhu & Woodcock, 2012; Zhu et al., 2015), employ dynamic thresholds derived from object-based cloud and cloud shadow statistics. In our previous work (Chen et al., 2014), a model based dynamic threshold method was developed, tested, and shown to have superior performance compared to the MODIS MOD35 algorithm over the snow-covered Greenland Plateau.

Because of the similarity of cloud and snow/ice optical properties in VIS and near NIR channels, snow detection has always been essential in cloud mask algorithm designs. Indices for mapping snow cover using VIS and SWIR data were developed in the mid-1970s. The Normalized Difference Snow Index (NDSI) was introduced by Hall et al. (1995) to map snow using MODIS data. Prior to that, Dozier (1987, 1989) used a VIS/SWIR index algorithm to map snow based on Landsat data. Most threshold-based cloud mask algorithms will use NDSI in their processing chain (Ackerman et al., 1998, 2010; Irish et al., 2006; Zhu & Woodcock, 2012) for cloud screening, which highlights the importance of snow detection since its accuracy will also affect that of cloud detection.

Enhanced computational power and improvements in machine learning techniques have allowed machine learning algorithms, such as decision trees, logistic regressions, support vector machines, and artificial neural networks, to be used for cloud masking and snow/ice detection. Taravat et al. (2015) used a multi-layer perceptron neural network model to detect clouds in Landsat images. Hollstein et al. (2016) compared several methods, including decision tree, classical Bayesian, random forest, support vector machine, and stochastic gradient descent, applied to Sentinel-2 MultiSpectral Instrument (MSI) images. Hughes & Hayes (2014) used a neural network based method trained with a subset of the United States Geological Survey Landsat Data Continuity Mission (USGS LDCM) Cloud Cover Assessment Data (Scaramuzza et al., 2012) and a comparison with fmask (Zhu & Woodcock, 2012) showed favorable results.

Bayesian methods have shown significant improvements over threshold based methods. Notably, model based Bayesian statistical methods have shown that simulated datasets can be used as a predictor to improve the cloud detection accuracy. Merchant et al. (2005) first applied this method for cloud screening over ocean areas in order to retrieve sea surface temperature. Bulgin et al. (2014), and Bulgin et al. (2018) extended this method to be applied over land areas. In these studies, manually classified datasets were used for validation. An automatic Bayesian classifier, derived using collocated AVHRR and CALIOP data by Andrew K. Heidinger et al. (2012), showed improvements over threshold-based methods and the ability to derive uncertainties in the cloud masking process. The dependence on CALIOP data to derive posterior cloud probability was also introduced in this paper.

Recently, a support vector machine (SVM) approach has been used in the latest CLAUDIA3 algorithm (Ishida et al., 2018). High quality training datasets are essential to machine-learning-based methods and manually-generated datasets such as the ACCA reference dataset (Irish et al., 2006) and the Sentinel-2 MSI dataset constructed by Hollstein et al. (2016) are often used by current machine-learning-based cloud detection schemes. In Ishida et al. (2018) the training dataset for the SVM classification is also selected subjectively from actual satellite measurements by carefully examining the typical surface type and eliminating irregular data.

1.2. Limitations of traditional methods

Traditional threshold-based cloud mask methods still face serious challenges over snow- and ice-covered areas, especially in Arctic and sub-arctic regions where there are frequent temperature inversions (affecting TIR-based tests) and over mid-latitude regions where the reflected signal is often from pixels with mixed snow and vegetation/soil cover. In order to handle such complicated surface conditions, the threshold-based logic becomes increasingly complex (as can be seen in plates 1-5 of Irish et al. 2006) and a large number of satellite channels is often required. Sometimes these tests will produce conflicting results and additional "clear restoral tests" are needed (Ackerman et al., 2010) to avoid mis-classification. The need to detect possible snow-covered areas also adds uncertainty to the results. As reported by Wang et al. (2008), mis-classifications of snow-covered areas as "cloud" or vice versa are still a serious problem in results produced by traditional threshold-based methods such as the MODIS cloud mask as will be shown in Section 3.

Machine learning methods, on the other hand, generally have no dependence on thresholds and do not rely on detecting snow before cloud screening. However, the dependence on manually-generated datasets has limited the development and operational use of machine learning based algorithms. It is difficult to generate a reliable training dataset due to the large amount of human resources needed to classify hundreds of images with millions of pixels. The limited amount of manually-classified images also makes it hard to cover all possible solar/viewing geometries, which limits the operational use of trained algorithms. Most importantly, manually-classified images are usually available only post-launch. This circumstance impedes pre-launch evaluation of algorithm performance and makes its application to a different sensor difficult.

2. New approach

In this paper, we present a new machine-learning based approach to cloud and snow detection and discrimination to overcome the limits of previous methods. Instead of using manually-generated datasets, we simulate the training dataset needed by machine learning algorithms. Compared to manually-generated training data based on actual measurements, simulated training data have the following advantages:

- There is no need for humans to identify hundreds of images with millions of pixels, which greatly saves human effort.
- The number of training samples can be as large as desired/needed, which can help avoid overfitting problems and be used to fully explore the potential of machine learning techniques.
- The training dataset can cover the full range of possible solar/viewing geometries.
- The algorithm can easily be modified for application to different sensors; only new training datasets are needed.

In order to create such a training dataset, it is necessary to take into account the interaction of incident solar radiation with different types of surfaces, aerosols and clouds. This requirement implies that it is crucially important to have access to a comprehensive radiative transfer model. In order to simulate the reflectance from complex land surfaces, we constructed such a model; the details are provided in the following section.

2.1. Radiative transfer simulations

In order to simulate the light signal received by a satellite instrument, we need to solve the radiative transfer equation (RTE) pertinent for light propagation in the coupled atmosphere-surface system. The diffuse radiance $I(\tau, \theta, \phi)$ at wavelength λ is found by solving the following RTE:

$$\begin{aligned}\mu \frac{dI(\tau,\theta,\phi)}{d\tau} =& I(\tau,\theta,\phi) - \frac{\varpi(\tau) F_0 e^{-\tau/\mu_0}}{4\pi} p(\tau,\theta',\phi';\theta_0,\phi_0) \\ & - \frac{\varpi(\tau)}{4\pi} \int_0^{2\pi} d\phi' \int_{-1}^{1} d\mu' p(\tau,\theta',\phi';\theta,\phi) I(\tau,\theta',\phi').\end{aligned} \tag{1}$$

Here F_0 is the incident top-of-the-atmosphere (TOA) solar irradiance (normal to the beam), while the differential optical depth $d\tau = -(\alpha + \beta)dz$, the single scattering albedo $\varpi = \beta/(\alpha + \beta) = \beta/\gamma$, and the scattering phase function $p(\tau, \theta', \phi'; \theta, \phi)$ are the inherent optical properties (IOPs) of the scattering/absorbing medium. Note that we have used the Greek letters α, β, and $\gamma = \alpha + \beta$ to denote the absorption, scattering, and extinction coefficients, respectively. θ_0 and ϕ_0 represent solar zenith and azimuth angles, $\mu_0 = \cos\theta_0$; θ' and ϕ' are sensor zenith and azimuth angles prior to a scattering event, and θ and ϕ the corresponding angles after the scattering event, $\mu = \cos\theta$. In our training dataset, the TOA bidirectional reflectance factor (hereafter simply referred to as the reflectance), defined as $R(\tau, \theta, \phi) = \pi I(\tau, \theta, \phi)/F_0 \cos\theta_0$, is simulated using the latest version of the DISORT radiative transfer model (RTM) (DISORT 4.0, Lin et al. 2015; Stamnes et al. 1988, 2017) employing the sub-band IOP method developed by Chen et al. (2017) to improve the accuracy in SWIR channels.

2.1.1. Atmosphere IOPs

We used the U.S. Standard atmosphere constituent profiles (Anderson et al., 1986) divided into 14 layers to provide input to a band model based on MODTRAN [see for example, Stamnes et al. (2017) for details] to generate absorption coefficients and optical depths due to atmospheric trace gases including H_2O,

CO_2, O_3, CH_4, and NO_2. Layering is needed to resolve the vertical variation in the IOPs, and experience has shown that 14 layers is sufficient for this purpose. Molecular (Rayleigh) scattering optical depths are computed from the Rayleigh scattering cross section (Stamnes et al., 2017) multiplied by the bulk density of air available from Anderson et al. (1986). The aerosol IOPs are tabulated from the output of the OPAC aerosol model (Hess et al., 1998). Liquid water clouds are assumed to consist of a polydispersion of spherical particles and the IOPs are calculated from Mie-Debye theory (Mishchenko et al., 2002) using the refractive index of water from Segelstein (1981). For ice clouds the IOPs are tabulated from the "general habit mixture" model in the bulk scattering and absorption models of Baum et al. (2011). Clouds are assumed to have a thickness of 2 km. The cloud base height is assumed to be 2 km above the surface for liquid water clouds. For ice clouds the cloud base height is assumed to be at 8 km regardless of the surface elevation.

2.1.2. Surface IOPs

In order to simulate the TOA reflectance from different land surface types, we used the Soil-Leaf-Canopy (SLC) model (Verhoef & Bach, 2007) in conjunction with our DISORT RTM. The bidirectional reflectance distribution function (BRDF) output from the SLC model is used as the lower boundary condition in DISORT. Figure 1 shows the bottom-of-the-atmosphere (BOA) reflectance in the nadir direction of different types of green and brown vegetation with underlying soil type = 1 (representing a type of ploughed soil) as simulated by the SLC model. By changing the parameters such as the Leaf Area Index (LAI), brown vegetation fraction (f_b) or soil type, the reflectance from various types of green/brown vegetations as well as bare soil can be simulated. Snow particles were assumed to be ice spheres with the refractive index of ice obtained from Warren & Brandt (2008). The monochromatic IOPs can be calculated from Mie-Debye theory once the size distribution is specified or from a parameterization in terms of effective snow grain size (Stamnes et al., 2011).

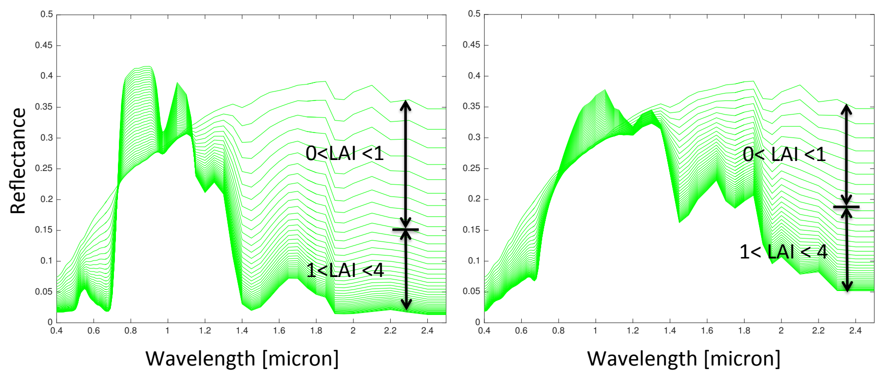

Figure 1: Bottom-of-the-atmosphere (BOA) spectral reflectance in the nadir direction as a function of LAI from green vegetation (left) and brown vegetation (right). The incident solar zenith angle was set to 30° in these simulations.

2.1.3. Reflectance for mixed snow/vegetation/soil cases and high elevation areas

In order to better handle the case of fractional snow cover, we adopted the following linear mixing rule for the reflectance of pixels with snow fraction, f:

$$R_{\text{mix}} = (1 - f) \times R_{\text{land}} + f \times R_{\text{snow}}.$$

By randomly changing the snow fraction f and snow/land parameters, we can simulate the TOA reflectance for a variety of snow-mixed-vegetation/soil cases. In order to handle the change of TOA reflectance with surface elevation, we simulated the TOA reflectance by assuming the surface elevation to be at randomly generated heights between 0 and 1000 m. For snow areas at very high elevations such as in Greenland and Antarctica, we extended the surface elevation range in our simulations to be between 0 and 4000 m.

2.1.4. TOA reflectance for clear-sky and cloudy cases

Figure 2 shows examples of TOA reflectances obtained from our radiative transfer simulations for different surface types under different cloud optical depths (COD). It can be seen that cloudy cases have different TOA reflectances, which depend on the underlying surface type. Due to highly conservative nature of cloud scattering in the VIS and NIR wavelength region (single-scattering albedo close to 1 for cloud particles, see for example Yang et al. 2013), a considerable amount of solar radiation will reach the surface even for a moderately thick cloud (optical depth of 10) and the reflected signal from the surface will contribute significantly to the TOA reflectance (see for example Chapter 13 of Petty 2006 for details). Hence, the inclusion of surface reflection is very important for cloudy-sky simulations. In the latest MODIS Collection 6 cloud products (Amarasinghe et al., 2017), a Cox-Munk based surface BRDF model was used to account for the significant contribution from the ocean surface. Over land the surface was assumed to act as a Lambertian reflector, so that the total reflectance can be expressed as a sum of the value for a black surface plus an algebraic correction term proportional to the Lambertian surface albedo (see Eq. (5) in Amarasinghe et al. 2017), which may lead to significant errors when the BRDF of the underlying surface is very anisotropic (such as for snow). In our radiative transfer simulation dataset a rigorous surface BRDF treatment is implemented for vegetation, soil, and snow, which avoids the potential problem of assuming Lambertian reflection from the land surface. The dependence of the TOA reflectance on surface reflectance also means that we need to cover as many surface types as possible to establish a comprehensive dataset, which can represent most cases, and this diversity could be a challenge to our machine learning scheme. One can also observe that for very thin clouds (cloud optical depth < 0.5) the change in reflectance compared to the clear-sky cases is usually very small. This circumstance indicates a possible limitation of cloud detection using reflectance channels and that thermal infrared channels may be needed to distinguish such thin clouds from the underlying surface.

2.2. Neural network training

The training dataset for our machine-learning based algorithm consists of a large number of clear-sky and cloudy cases designed to cover as many surface types and solar/viewing geometries as desired for adequate representation of possible combinations encountered in nature. Atmosphere and surface pa-

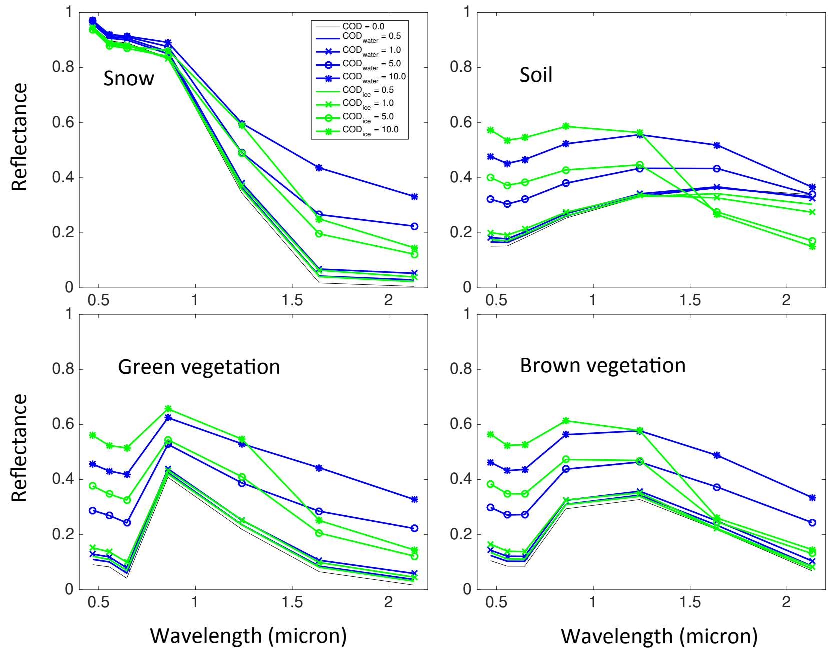

Figure 2: Simulated MODIS TOA spectral reflectance in the nadir direction for different clear sky (COD = 0.0) and cloudy cases (COD > 0.0). The surface types are snow (top left), soil (top right), green vegetation (bottom left) as well as brown vegetation (bottom right). The cloud optical depths were assumed to be 0.5, 1.0, 5.0 and 10.0 at 555 nm wavelength. The incident solar zenith angle was set to 30° in these simulations.

rameters such as aerosol/cloud optical depth, leaf area index (LAI), fraction of brown vegetation (f_b), and snow grain size were considered to be free parameters allowed to vary within realistic ranges (see Table 1). For clear sky conditions a large number of different cases were randomly selected in order to represent a large variety of soil, vegetation, and aerosol combinations in the training dataset. Similarly, for any given surface and clear sky condition a large number of water/ice cloud optical depths were randomly selected to simulate corresponding TOA reflectances. The simulated reflectances in six satellite channels (0.47, 0.55, 0.66, 0.86, 1.24, 2.13 μm, for MODIS/Aqua) obtained in this manner, together with solar zenith, viewing zenith, relative azimuth angle, and surface elevation serve as the input parameters to the algorithm.

Parameter	range	unit	comment
SZA	0.0 - 85.0	degrees	solar zenith angle
VZA	0.0 - 65.0	degrees	viewing zenith angle
RAZ	-180.0 - 180.0	degrees	relative azimuth angle
LAI	0.0 - 4.0		leaf area index
f_b	0.0 - 1.0		brown vegetation fraction
soil code	0 - 22		soil type in SLC model
AOD	0.0 - 1.0		aerosol optical depth
COD_w	0.5 - 50.0		cloud optical depth (water clouds)
COD_i	0.5 - 20.0		cloud optical depth (ice clouds)
$\mathrm{r}_{\mathrm{eff}}$	50 - 2000	μm	snow grain size
f	0.0 - 1.0		snow fraction

Table 1: Parameters and their range in the training dataset.

In this way, over 20 million samples were generated and used to train a binary (cloudy/clear) neural network classifier employing a simple multilayer perceptron scheme with one hidden layer of 10 neurons. The sigmoid function $\sigma = 1/(1+e^{-z})$ was used as the activation function for all layers. We performed random permutations to our dataset and then divided it into two parts: 75% of the total number of cases was used in training and the remaining 25% was used in validation. After a sufficient number of iterations (usually about 200) the accuracy for both the training and validation dataset was usually between 98.5% and 99.2%, which means that we had achieved adequate accuracy while avoiding overfitting. The trained neural network can process one MODIS image (which typically contains $2030\times1354 = 2.7$M pixels) in less than two seconds. The main parameters of the simulations and their range of variation are listed in Table 1 and a flowchart of the new Snow-ice Cloud mask (SCM) algorithm is shown in Fig. 3.

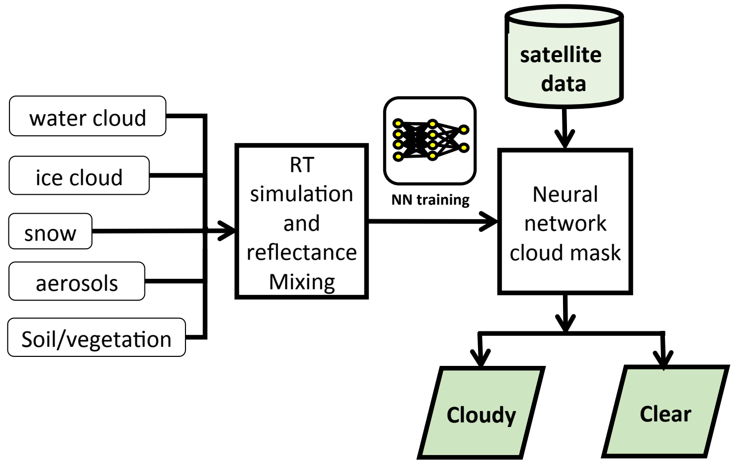

Figure 3: Flowchart of the SCM algorithm.

3. Results and validation

In this section we will apply the trained neural network classifier to MODIS images and validate its performance over different land regions. We first tested the SCM using the aforementioned 6-channel configuration to simulate its performance on sensors such as the Second-Generation Global Imager (SGLI) on GCOM-C (Japan) and Visible Infrared Imaging Radiometer Suite (VIIRS) on board the Suomi National Polar-orbiting Partnership (Suomi NPP) weather satellite. In comparison to MODIS these sensors lack many TIR bands so that the performance achieved by using mainly reflectance bands becomes a matter of significant importance. However, since SGLI has two thermal IR bands (11 and 12 μm) we also explored the advantage of employing a dynamic threshold split-window test similar to that used by Wilson & Oreopoulos (2013) (Figure 2) to improve the sensitivity to thin cirrus clouds.

3.1. Results over Mid-latitude land areas: Comparison with MODIS images

Figure 4 shows some examples of cloud detection results produced by SCM and comparisons with similar results produced by Collection 6 of the MODIS cloud mask (MOD35 C6). The clouds detected by MOD35 are shown in white (confident cloudy) and grey (probably cloudy) colors. The cloud detection by the SCM algorithm is binary, which means that only cloudy (shown in white) and clear-sky over land (shown in green) identifications are provided. A color scheme (using MODIS channel 1-6-32 as R-G-B) identical to that of Hutchison et al. (2013) was used for false color RGB plots in Fig. 4. In this scheme, clouds generally look white (warm low clouds) and yellow (cold ice clouds), while snow-covered areas usually look pink, due to their relatively low SWIR reflectance compared to that of clouds.

From the comparisons, one can see that in general SCM and MOD35 C6 have similar cloud detection capabilities over non-snow-covered land areas, which include vegetated land areas over Europe and the Sahara desert in North Africa (bottom panels of Fig. 4). These comparisons show that the neural network based SCM algorithm can capture the spectral signature of various land surfaces including various types of vegetation as well as bright desert areas and distinguish them from clouds. Such discrimination was typically difficult for many previously employed cloud mask algorithms. For pure snow-covered areas such as the Greenland Plateau, the performance of SCM and MOD35 are also similar (the top panels of Fig. 4), which means that the neural networks employed in SCM perform well over high-elevation snow-covered areas. The decline in performance for both algorithms in spring/autumn seasons is probably due to the very high solar zenith angles (usually greater than 80°) and reduced number of samples. However, the situation changes over snow-covered areas in mid-latitude regions. In the middle panels of Fig. 4 one can see that large amounts of clear-sky snow pixels (pink in false color RGB) are mis-classified as cloudy pixels by MOD35 whereas SCM provides correct identifications. The complicated snow-vegetation-soil mixing conditions created considerable difficulty for the threshold tests in the MOD35 algorithm, as one can see that the mis-classifications are mostly along the edges of snow areas.

3.2. Statistical validation using CALIOP

The validation of previous machine learning based algorithms is limited to image-based statistics based on use of human-identified images selected from different locations and seasons as benchmarks. Due to the large amount of pixels to be classified by humans, it is difficult to achieve the spatial and temporal coverage needed for a comprehensive evaluation of the effectiveness of a cloud mask algorithm. The Cloud-Aerosol Lidar with Orthogonal Polarization (CALIOP) is a lidar onboard the CALIPSO satellite that provides high-resolution vertical profiles of aerosols and clouds. CALIOP's active cloud detection scheme combined with collocated Aqua MODIS data provide the most reliable assessment of cloud mask results currently available. We used collocated CALIOP and Aqua MODIS measurements employing CALIOP-detected cloudy/clear conditions for comparison in a similar manner as we did in Chen et al. (2014) over the snow-covered Greenland Plateau. Hence, the CALIOP 1 km cloud detection results were used as benchmarks. The whole year datasets for 2008 over East Asia, Europe, North America, and Greenland were used. The approximate areas covered by these MODIS images are indicated by the green boxes in Fig. 5 and roughly 2000 MODIS images were used for each site. Similar to what we did in Chen et al. (2014), we calculated and compared the hit rate (HR) and the Hanssen-Kuiper (True) Skill Score (TSS) of SCM and MOD35 (MYD35 for Aqua MODIS data). The HR and TSS are defined as

$$\mathrm{HR} = \frac{\mathrm{N_{cld,hit}} + \mathrm{N_{clr,hit}}}{\mathrm{N_{total}}} \tag{2}$$

and

$$\mathrm{TSS} = \frac{(\mathrm{N_{cld,hit}} \times \mathrm{N_{clr,hit}} - \mathrm{N_{cld,miss}} \times \mathrm{N_{clr,miss}})}{(\mathrm{N_{cld,hit}} + \mathrm{N_{cld,miss}}) \times (\mathrm{N_{clr,hit}} + \mathrm{N_{clr,miss}})}, \tag{3}$$

where $\mathrm{N_{cld,hit}}$, $\mathrm{N_{clr,hit}}$, $\mathrm{N_{clr,miss}}$, and $\mathrm{N_{cld,miss}}$ are defined in Table 2.

Figure 6 as well as Table 3 show CALIOP validation results of SCM and MOD35. We included the results obtained by using the neural network only labeled "SCM (NN + only)" in Fig. 6. In general, the neural network test in SCM performs consistently over non-snow covered areas, achieving about 80% HR and 65% TSS. Adding the thermal IR test can improve the HR and

Scenario	SCM/MYD35 clear	SCM/MYD35 cloudy
CALIOP clear	$N_{clr,hit}$	$N_{clr,miss}$
CALIOP cloudy	$N_{cld,miss}$	$N_{cld,hit}$

Table 2: Contingency matrix of CALIOP versus SCM/MYD35.

TSS by 5% to 7%, but the performance is slightly lower compared to MOD35. These results indicate that there is some room for improvement of the SCM over non-snow covered areas, and the additional tests using bands in thermal IR wavelength range can significantly improve the identification of thin clouds, which are difficult to identify solely by reflectance-based methods.

Over the snow-covered Greenland Plateau area the two algorithms perform very closely with SCM (NN + BT) having a slight advantage during the summer months. The advantage of adding the thermal IR test is relatively small, probably due to the conservative thresholds used. We found that it is insufficient to use only 2 thermal channels (10.8 and 12 μm) over the snow-covered Greenland Plateau and that more thermal IR channels such as the 3.7 μm is probably needed to further improve the result. The drop in both HR and TSS in the winter months may be associated with the reduced number of samples and larger solar zenith angles in these months. The biggest difference is again found in mid-latitude areas during the winter season, where snow is frequently mixed with vegetation and soil. The TSS scores of MOD35 show a significant drop due to a much higher mis-classification rate of clear-sky cases, consistent with our image-based test results showing that MOD35 has difficulty handling complex snow-mixed-vegetation/soil scenes. It should be noted that sometimes MOD35 has a higher HR but a lower TSS compared to SCM (such as in January over North America). This behavior is due to the bias in the HR since there are generally more cloudy than clear-sky cases in our statistical sample, and the more comprehensive TSS captured the increase of $N_{clr,miss}$, which leads to a mis-classification of clear-sky as cloudy cases by MYD35 compared to SCM in winter months, as seen in Table 3.

3.3. Performance of a 3-channel configuration like the AVHRR-3 sensor

Finally, we tested a special configuration to investigate the flexibility of the SCM for application to other sensors. Thus, instead of using the above mentioned six MODIS reflectance channels, we tried a 3-channel configuration (0.47, 0.66, and 2.13 μm) for the training of our algorithm in order to simulate its application to legacy sensors such as AVHRR-3. Figure 7 shows that this 3-channel configuration can provide consistent although slightly inferior performance compared to the 6-channel configuration. These 3-channel results are still better than those provided by MOD35 in mid-latitude areas during the winter season. The use of simulated data for training allows us to assess the performance of algorithms based on machine learning techniques before the launch of a satellite, and to explore the most effective combinations of satellite channels to be used for cloud masking.

4. Discussion

The SCM cloud screening tool described above is our first attempt to use a scheme based on comprehensive radiative transfer simulations combined with machine learning for cloud screening. Based on our experience gained so far with this methodology, we believe there are many aspects of this approach that can be improved. These include:

- Constructing localized training datasets of clear-sky simulations which depends on local atmospheric and surface conditions. The current training dataset was simulated using fixed atmospheric constituent profiles as well as using randomly generated surface properties (soil type, green-brown vegetation ratio). Hence, in this paper, we have described a general application of the method using a generic set of atmospheric and surface parameters to demonstrate its usefulness on a global scale. In further applications it is completely possible to construct a training dataset that employs local surface parameters (soil type, vegetation type) if these pa-

Table 3: SCM and MYD35 statistics using CALIOP as the benchmark.

Month	Location	Total pixel	SCM statistics						MYD35 statistics					
			$N_{clr,hit}$	$N_{clr,miss}$	$N_{cld,hit}$	$N_{cld,miss}$	HR(%)	TSS(%)	$N_{clr,hit}$	$N_{clr,miss}$	$N_{cld,hit}$	$N_{cld,miss}$	HR(%)	TSS(%)
Jan.	GNL[a]	0	0	0	0	0	N/A	N/A	0	0	0	0	N/A	N/A
	EU[b]	53731	14180	906	32737	5908	87.32	78.71	10152	4934	36748	1897	87.29	62.39
	EA[c]	57678	27840	2504	19320	8014	81.76	62.43	16401	13943	25073	2261	71.91	45.78
	NA[d]	78123	26453	1414	38664	11592	83.35	71.86	18796	9071	47014	3242	84.24	61.00
Feb.	GNL	0	0	0	0	0	N/A	N/A	0	0	0	0	N/A	N/A
	EU	71145	19090	1220	41299	9536	84.88	75.23	15098	5212	47723	3112	88.30	68.22
	EA	54456	29204	2997	16460	5795	83.85	64.65	17225	14976	20397	1858	69.09	45.14
	NA	89715	35176	1749	38367	14423	81.97	67.94	24921	12004	48547	4243	81.89	59.45
Mar.	GNL	31135	12902	3619	10116	4498	73.93	47.32	11646	4875	10326	4288	70.57	41.15
	EU	54593	13883	841	32227	7643	84.46	75.12	11323	3401	36845	3025	88.23	69.31
	EA	39387	13667	1433	19737	4550	84.81	71.78	11912	3188	21603	2684	85.09	67.84
	NA	71863	28065	2085	29350	12363	79.90	63.45	21542	8608	36258	5455	80.43	58.37
Apr.	GNL	41903	19858	2797	11270	7978	74.29	46.21	20224	2431	11552	7696	75.83	49.29
	EU	76635	24105	1115	41869	9546	86.09	77.01	21196	4024	46032	5383	87.72	73.57
	EA	55684	16782	1888	30687	6327	85.25	72.79	16209	2461	31757	5257	86.14	72.62
	NA	94116	37586	2235	40793	13502	83.28	69.52	33106	6715	47331	6964	85.47	70.31
May	GNL	54366	23425	2455	18849	9637	77.76	56.68	22085	3795	20692	7794	78.68	57.98
	EU	82032	25991	1615	44552	9874	85.99	76.01	24448	3158	47778	6648	88.05	76.35
	EA	57357	16312	1903	33385	5757	86.65	74.84	16651	1564	33704	5438	87.79	77.52
	NA	103848	30967	2325	58931	11625	86.57	76.54	29113	4179	63180	7376	88.87	76.99
Jun.	GNL	47081	17461	1740	20878	7002	81.43	65.82	16430	2771	22170	5710	81.99	65.09
	EU	59560	19495	1434	31962	6669	86.40	75.88	19031	1898	33756	4875	88.63	78.31
	EA	41193	9213	1527	26882	3571	87.62	74.06	9749	991	27041	3412	89.31	79.57
	NA	78078	26079	2180	41140	8679	86.09	74.86	25176	3083	43332	6487	87.74	76.07
Jul.	GNL	52804	21032	1175	23877	6720	85.05	72.75	19402	2805	25375	5222	84.80	70.30
	EU	73924	28486	1849	34569	9020	85.30	73.21	27905	2430	37228	6361	88.11	77.40
	EA	50247	12268	2125	30803	5051	85.72	71.15	12768	1625	30986	4868	87.08	75.13
	NA	92489	33188	1976	46690	10995	86.03	75.32	31985	3179	48957	8728	87.18	75.83
Aug.	GNL	40431	13844	740	21069	4778	86.35	76.44	13214	1370	21707	4140	86.37	74.59
	EU	78525	29104	1318	38179	9924	85.68	75.04	28528	1894	41570	6533	89.27	80.19
	EA	53886	16900	1698	29138	6150	85.44	73.44	17025	1573	30160	5128	87.56	77.01
	NA	98767	37118	1557	48122	11970	86.30	76.05	36433	2242	51096	8996	88.62	79.23
Sep.	GNL	28970	7412	1008	16065	4485	81.04	66.20	7157	1263	16200	4350	80.62	63.83
	EU	60527	15230	578	38856	5863	89.36	83.23	14503	1305	41627	3092	92.74	84.83
	EA	45895	16739	1454	23243	4459	87.12	75.91	16259	1934	24197	3505	88.15	76.72
	NA	73406	24993	1117	38205	9091	86.09	76.50	23989	2121	42030	5266	89.94	80.74
Oct.	GNL	21176	6296	1818	9966	3096	76.79	53.89	6136	1978	10384	2678	78.01	55.12
	EU	75555	20031	655	45596	9273	86.86	79.93	18513	2173	50542	4327	91.60	81.41
	EA	54653	21731	1202	25932	5788	87.21	76.51	19753	3180	28048	3672	87.46	74.56
	NA	92471	32706	771	46849	12145	86.03	77.11	30827	2650	53204	5790	90.87	82.27
Nov.	GNL	0	0	0	0	0	N/A	N/A	0	0	0	0	N/A	N/A
	EU	61436	18634	1087	35752	5963	88.52	80.19	15643	4078	39627	2088	89.96	74.32
	EA	56730	30393	1298	18848	6191	86.80	71.18	24315	7376	22612	2427	82.72	67.03
	NA	86324	24965	739	49112	11508	85.81	78.14	21513	4191	56644	3976	90.54	77.14
Dec.	GNL	0	0	0	0	0	N/A	N/A	0	0	0	0	N/A	N/A
	EU	46213	10938	915	29789	4571	88.13	78.98	7681	4172	32843	1517	87.69	60.39
	EA	58278	30802	2317	18012	7147	83.76	64.60	19968	13151	22814	2345	73.41	50.97
	NA	77136	26854	471	37885	11926	83.93	74.33	19801	7524	46653	3158	86.15	66.12

a) GNL: Greenland

b) EU: Europe

c) EA: East Asia

d) NA: North America

rameters are known for the area of interest. It will also be useful to improve the dynamic range of the clear sky simulations by introducing parameters such as relative humidity and atmospheric pressure. For applications to a given location for a given time of the year, it is possible to simulate a range of high accuracy clear-sky radiances to improve the discrimination.

- Constructing a more realistic training dataset of cloudy-sky simulations. In the current simulation dataset we have for simplicity employed a fixed cloud height (2.0 km above the surface for liquid water clouds, 8.0 km for ice clouds). In future implementations the cloud levels and properties can be made more flexible to improve the cloudy/clear sky determination. The use of simulation dataset in combination with human identified dataset will also be interesting to investigate.

- Adding additional thermal IR channels in the simulations. Currently we have not yet used simulations for thermal IR channels. Such simulations would involve a variety of different cloud properties as well as different surface emissivities. The use of thermal IR channels can not only help to improve the detection of optically thin clouds, but also extend our method to work during night time.

- Using additional machine learning techniques to improve the performance. In this paper, we used a simple perceptron neural network model to perform the cloudy/clear-sky determination because it is easy to train and implement. Other approaches, such as bagged decision trees, support vector machines, and/or Bayesian methods can also be used. In fact, preliminary tests indicate that a bagged tree model could achieve higher accuracy than the current neural network method. Testing/validation of such models using satellite data is currently in progress.

As discussed above, our methodology and algorithm can certainly be improved and it is important that users in the remote sensing community can help further explore this approach. We are planning to create a version of our current algorithm to be implemented (as a “plugin”) in ESA’s SNAP platform, and thereby make it available to the remote sensing community. We will also make our training dataset available on our website (http://lllab.phy.stevens.edu) to people who are interested in further exploring this methodology.

5. Summary

A cloud mask and snow detection algorithm (SCM), based on machine learning techniques, has been developed, described, and validated by collocated Aqua MODIS/CALIOP measurements over land areas. Instead of using a human-classified dataset derived from actual measurements, SCM uses a simulated dataset generated by extensive radiative transfer simulations to train the machine learning algorithm. Compared to traditional methods, such as the MODIS cloud mask or other previous machine learning based algorithms, this new algorithm has the following features:

- it simplifies the test logic and utilizes fewer satellite channels while being able to deliver consistent performance over different types of underlying surfaces in different seasons,
- it has a low mis-classification rate of clear-sky cases, which yields a significantly higher TSS score during the winter seasons over mid-latitude land areas when the surface is covered by snow mixed with vegetation/soil,
- it performs similarly to the MODIS cloud mask over pure vegetation, soil and snow-covered areas,
- it can easily be modified to be applicable to a new sensor configuration to assess its performance before the launch of a satellite because it relies entirely on simulated data for algorithm training. This feature facilitates exploring which satellite channels to use for cloud masking and retrieval of desired products before launch.

Finally, we should point out that the aim of JAXA's GCOM-C mission is to conduct global, long-term observations of the carbon cycle and radiation budget (Imaoka et al., 2010). The "Shikisai" satellite carrying GCOM-C was successfully launched in December 2017 and has started data transmission. The cloud mask algorithm described in this paper has been implemented in the data processing chain and will be used to retrieve cryospheric products consisting of key parameters such as snow grain size, impurity concentration as well as snow cover extent.

Acknowledgement: This work was conducted as a part of the GCOM-C1/SGLI algorithm development effort and was supported by the Japan Aerospace Exploration Agency (JAXA). We also want to thank the personnel at Space Science and Engineering Center of University of Wisconsin-Madison. Their publicly available CALMOD15 program, which provides accurate and efficient collocation of CALIOP and MODIS Aqua measurements makes the statistical validation of cloud mask algorithms possible. Finally, we would like to thank the MODIS and CALIPSO Teams for MODIS and CALIOP data and related data products, as well as the GSFC DAAC MODIS Data Support Team and ASDC Data Management Team for making MODIS and CALIOP data available to the user community.

6. Front matter

References

Ackerman, S., Frey, R., Strabala, K., Liu, Y., Gumley, L., & Baum, B. (2010). *Discriminating clear-sky from cloud with MODIS Algorithm Theoretical Basis Document (MOD35)*. Technical Report October Cooperative Institute for Meteorological Satellite Studies, University of Wisconsin - Madison.

Ackerman, S. A., Strabala, K. I., Menzel, W. P., Frey, R. A., Moeller, C. C., & Gumley, L. E. (1998). Discriminating clear sky from clouds with MODIS. *Journal of Geophysical Research*, *103*, 32141. doi:10.1029/1998JD200032.

Amarasinghe, N., Platnick, S., Meyer, K., & GSFC Cloud Retrieval Product Team (2017). *Overview of the MODIS Collection 6 Cloud Optical Property (MOD06) Retrieval Look-up Tables*. Technical Report.

Anderson, G. P., Clough, S. A., Kneizys, F. X., Chetwynd, J. H., & Shettle., E. P. (1986). *AFGL atmospheric constituent profiles (0-120km), AFGL-TR-*

86-0110 (OPI). Optical Physics Division, Air Force Geophysics Laboratory Hanscom AFB, MA 01736.

Andrew K. Heidinger, Evan, A. T., Foster, M. J., & Walter, A. (2012). A Naive Bayesian Cloud-Detection Scheme Derived from CALIPSO and Applied within PATMOS-x. *Journal of Applied Meteorology and Climatology*, *51*, 1129–1144. doi:10.1175/JAMC-D-11-02.1.

Baum, B. A., Yang, P., Heymsfield, A. J., Schmitt, C. G., Xie, Y., Bansemer, A., Hu, Y.-X., & Zhang, Z. (2011). Improvements in shortwave bulk scattering and absorption models for the remote sensing of ice clouds. *Journal of Applied Meteorology and Climatology*, *50*, 1037–1056. doi:10.1175/2010JAMC2608.1.

Bulgin, C., Sembhi, H., Ghent, D., Remedios, J., & Merchant, C. (2014). Cloud-clearing techniques over land for land-surface temperature retrieval from the advanced along-track scanning radiometer. *International Journal of Remote Sensing*, *35*, 3594–3615. doi:10.1080/01431161.2014.907941.

Bulgin, C. E., Mittaz, J. P. D., Embury, O., Eastwood, S., & Merchant, C. J. (2018). Bayesian cloud detection for 37 years of advanced very high resolution radiometer (avhrr) global area coverage (gac) data. *Remote Sensing*, *10*. doi:10.3390/rs10010097.

Chen, N., Li, W., Tanikawa, T., Hori, M., Aoki, T., & Stamnes, K. (2014). Cloud Mask Over Snow/ice Covered Areas for the GCOM-C1/SGLI Cryosphere Mission: Validations over Greenland. *Journal of Geophysical Research: Atmospheres*, . doi:10.1002/2014JD022017.

Chen, N., Li, W., Tanikawa, T., Hori, M., Shimada, R., Aoki, T., & Stamnes, K. (2017). Fast yet accurate computation of radiances in shortwave infrared satellite remote sensing channels. *Optics Express*, *25*, 443–451.

Dozier, J. (1987). Remote sensing of snow characteristics in the southern Sierra Nevada. In *Large Scale Effects of Seasonal Snow Cover* 166.

Dozier, J. (1989). Spectral Signature of Alpine Snow Cover from the Landsat Thematic Mapper. *Remote Sensing of Environment*, *22*, 9–22.

Hall, D. K., Riggs, G. A., & Salomonson, V. V. (1995). Development of Methods for Mapping Global Snow Cover Using Moderate Resolution Imaging Spectroradiometer Data. *Remote Sensing of Environment*, *34*, 127–140.

Hess, M., Koepke, P., & Schult, I. (1998). Optical Properties of Aerosols and Clouds: The Software Package OPAC. *Bulletin of the American Meteorological Society*, *79*, 831–844. doi:10.1175/1520-0477(1998)079<0831:OPOAAC>2.0.CO;2.

Hollstein, A., Segl, K., Guanter, L., Brell, M., & Enesco, M. (2016). Ready-to-Use Methods for the Detection of Clouds , Cirrus , Snow , Shadow , Water and Clear Sky Pixels in Sentinel-2 MSI Images, . (pp. 1–18). doi:10.3390/rs8080666.

Hughes, M., & Hayes, D. (2014). Automated detection of cloud and cloud shadow in single-date Landsat imagery using neural networks and spatial post-processing. *Remote Sensing*, *6*, 4907–4926. doi:10.3390/rs6064907.

Hutchison, K. D., Iisager, B. D., & Mahoney, R. L. (2013). Enhanced snow and ice identification with the VIIRS cloud mask algorithm. *Remote Sensing Letters*, *4*, 929–936. doi:10.1080/2150704X.2013.815381.

Imaoka, B. K., Kachi, M., Fujii, H., Murakami, H., Hori, M., Ono, A., Igarashi, T., Nakagawa, K., Oki, T., Honda, Y., & Shimoda, H. (2010). Global Change Observation Mission (GCOM) for Monitoring Carbon, Water Cycles, and Climate Change. *Preceedings of the IEEE*, *98*, 717–734.

Irish, R. R., Barker, J. L., Goward, S. N., & Arvidson, T. (2006). Characterization of the Landsat-7 ETM+ Automated Cloud-Cover Assessment (ACCA) Algorithm. *Photogrammetric Engineering & Remote Sensing*, *72*, 1179–1188. doi:10.14358/PERS.72.10.1179. arXiv:1103.1142v1.

Ishida, H., Oishi, Y., Morita, K., Moriwaki, K., & Nakajima, T. Y. (2018). Development of a support vector machine based cloud detection method for modis with the adjustability to various conditions. *Remote Sensing of Environment*, *205*, 390 – 407. doi:https://doi.org/10.1016/j.rse.2017.11.003.

Lin, Z., Stamnes, S., Jin, Z., Laszlo, I., Tsay, S.-C., Wiscombe, W., & Stamnes, K. (2015). Improved discrete ordinate solutions in the presence of an anisotropically reflecting lower boundary: Upgrades of the DISORT computational tool. *Journal of Quantitative Spectroscopy and Radiative Transfer*, *157*, 119 – 134. doi:http://dx.doi.org/10.1016/j.jqsrt.2015.02.014.

Merchant, C. J., Harris, A. R., Maturi, E., & Maccallum, S. (2005). Probabilistic physically based cloud screening of satellite infrared imagery for operational sea surface temperature retrieval. *Quarterly Journal of The Royal Meterological Society*, *131*, 2735–2755. doi:10.1256/qj.05.15.

Mishchenko, M. I., Travis, L. D., & Lacis, A. a. (2002). Scattering, Absorption, and Emission of Light by Small Particles. *NASA Goddard Institute for Space Studies, New York Institute for Space Studies, New York pace Studies, New York New York*, (pp. 1–486).

Petty, G. W. (2006). *A First Course in Atmospheric Radiation*. Sundog Publishing.

Scaramuzza, P. L., Bouchard, M. A., & Dwyer, J. L. (2012). Development of the landsat data continuity mission cloud-cover assessment algorithms. *IEEE Transactions on Geoscience and Remote Sensing*, *50*, 1140–1154. doi:10.1109/TGRS.2011.2164087.

Segelstein, D. J. (1981). The complex refractive index of water.

Stamnes, K., Hamre, B., Stamnes, J., Ryzhikov, G., Biryulina, M., Mahoney, R., Hauss, B., & Sei, a. (2011). Modeling of radiation transport in coupled atmosphere-snow-ice-ocean systems. *Journal of Quantitative Spectroscopy and Radiative Transfer*, *112*, 714–726. doi:10.1016/j.jqsrt.2010.06.006.

Stamnes, K., Thomas, G. E., & Stamnes, J. J. (2017). *Radiative transfer in the atmosphere and ocean*. (2nd ed.). Cambridge University Press.

Stamnes, K., Tsay, S. C., Wiscombe, W., & Jayaweera, K. (1988). Numerically stable algorithm for discrete-ordinate-method radiative transfer in multiple scattering and emitting layered media. *Applied optics*, *27*, 2502–9.

Stowe, L. L., Davis, P. A., & McClain, E. P. (1999). Scientific Basis and Initial Evaluation of the CLAVR-1 Global Clear / Cloud Classification Algorithm for the Advanced Very High Resolution Radiometer. *Journal of Atmospheric and Oceanic Technology*, *16*, 656–681. doi:10.1175/JCLI-D-12-00250.1.

Taravat, A., Proud, S., Peronaci, S., Del Frate, F., & Oppelt, N. (2015). Multilayer perceptron neural networks model for meteosat second generation SEVIRI daytime cloud masking. *Remote Sensing*, *7*, 1529–1539. doi:10.3390/rs70201529.

Verhoef, W., & Bach, H. (2007). Coupled soil-leaf-canopy and atmosphere radiative transfer modeling to simulate hyperspectral multi-angular surface reflectance and TOA radiance data. *Remote Sensing of Environment*, *109*, 166–182.

Wang, X., Xie, H., & Liang, T. (2008). Evaluation of modis snow cover and cloud mask and its application in northern xinjiang, china. *Remote Sensing of Environment*, *112*, 1497 – 1513. doi:https://doi.org/10.1016/j.rse.2007.05.016. Remote Sensing Data Assimilation Special Issue.

Warren, S. G., & Brandt, R. E. (2008). Optical constants of ice from the ultraviolet to the microwave: A revised compilation. *Journal of Geophysical Research*, *113*, D14220. doi:10.1029/2007JD009744.

Wilson, M. J., & Oreopoulos, L. (2013). Enhancing a Simple MODIS Cloud Mask Algorithm for the Landsat Data Continuity Mission. *IEEE Transactions* *on Geoscience and Remote Sensing*, *51*, 723–731. doi:10.1109/TGRS.2012.2203823.

Yang, P., Bi, L., Baum, B. a., Liou, K.-N., Kattawar, G. W., Mishchenko, M. I., & Cole, B. (2013). Spectrally Consistent Scattering, Absorption, and Polarization Properties of Atmospheric Ice Crystals at Wavelengths from 0.2 to 100 μ m. *Journal of the Atmospheric Sciences*, *70*, 330–347. URL: http://journals.ametsoc.org/doi/abs/10.1175/JAS-D-12-039.1. doi:10.1175/JAS-D-12-039.1.

Zhu, Z., Wang, S., & Woodcock, C. E. (2015). Improvement and expansion of the Fmask algorithm: Cloud, cloud shadow, and snow detection for Landsats 4-7, 8, and Sentinel 2 images. *Remote Sensing of Environment*, *159*, 269–277. doi:10.1016/j.rse.2014.12.014. arXiv:Zhu2015.

Zhu, Z., & Woodcock, C. E. (2012). Object-based cloud and cloud shadow detection in Landsat imagery. *Remote Sensing of Environment*, *118*, 83–94. doi:10.1016/j.rse.2011.10.028.

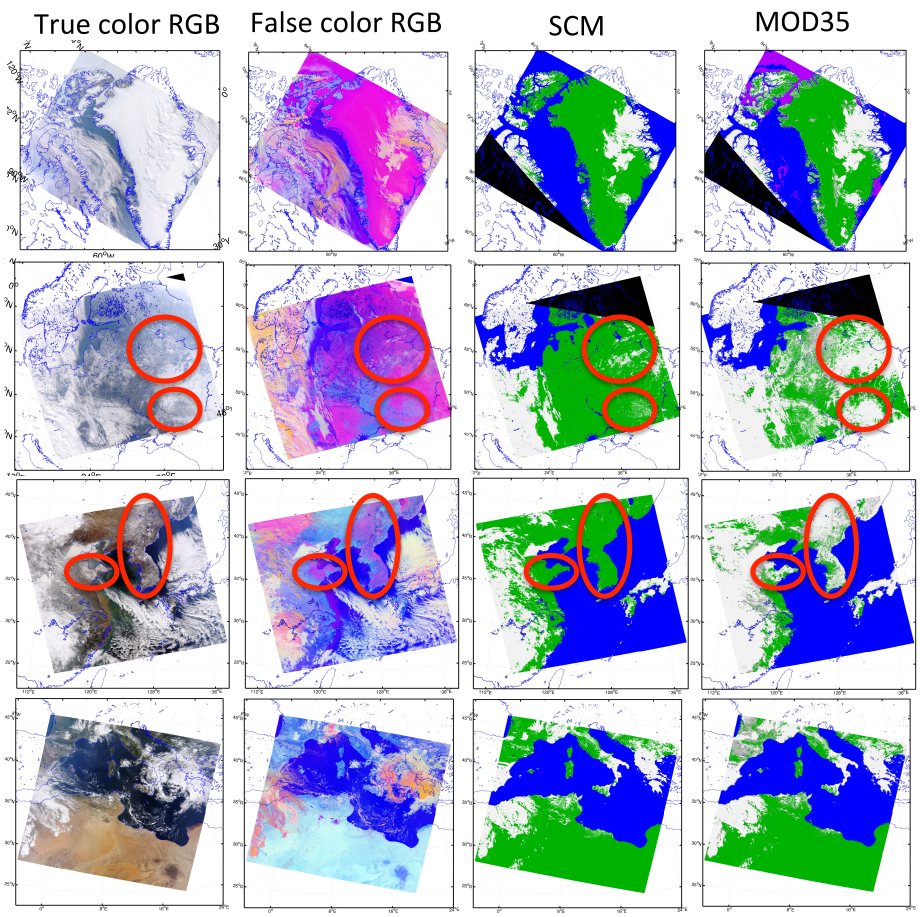

Figure 4: Cloud mask results for MODIS images. From top to bottom: Aqua MODIS image over Greenland, July 9, 2015; Aqua MODIS image over Europe, January 18, 2008; Aqua MODIS image over East Asia, January 24, 2003; Terra MODIS image over North Africa, September 26, 2009. False color RGB images are composed by using 0.65 μm and 2.13 μm reflectances and the 10.8 μm brightness temperature. Cloudy pixels are marked as white or grey, clear-sky land pixels as green, and water areas are maked as blue. Clouds over water areas are not marked.

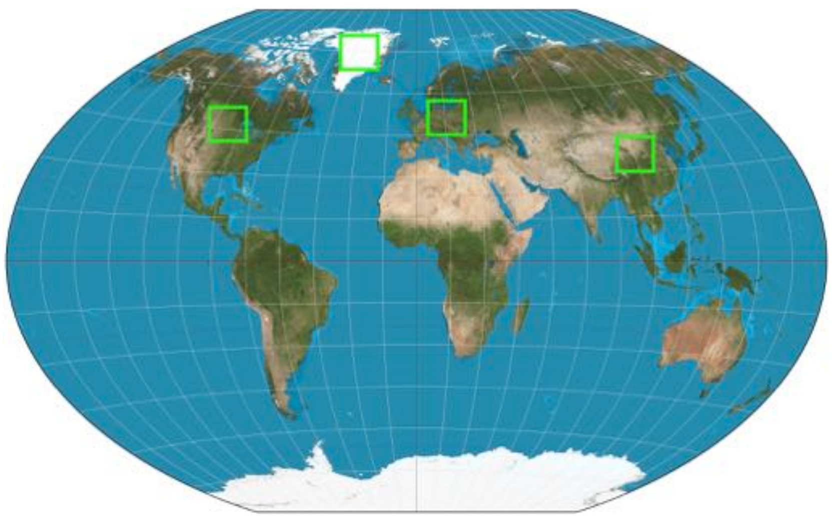

Figure 5: Validation areas used in this study.

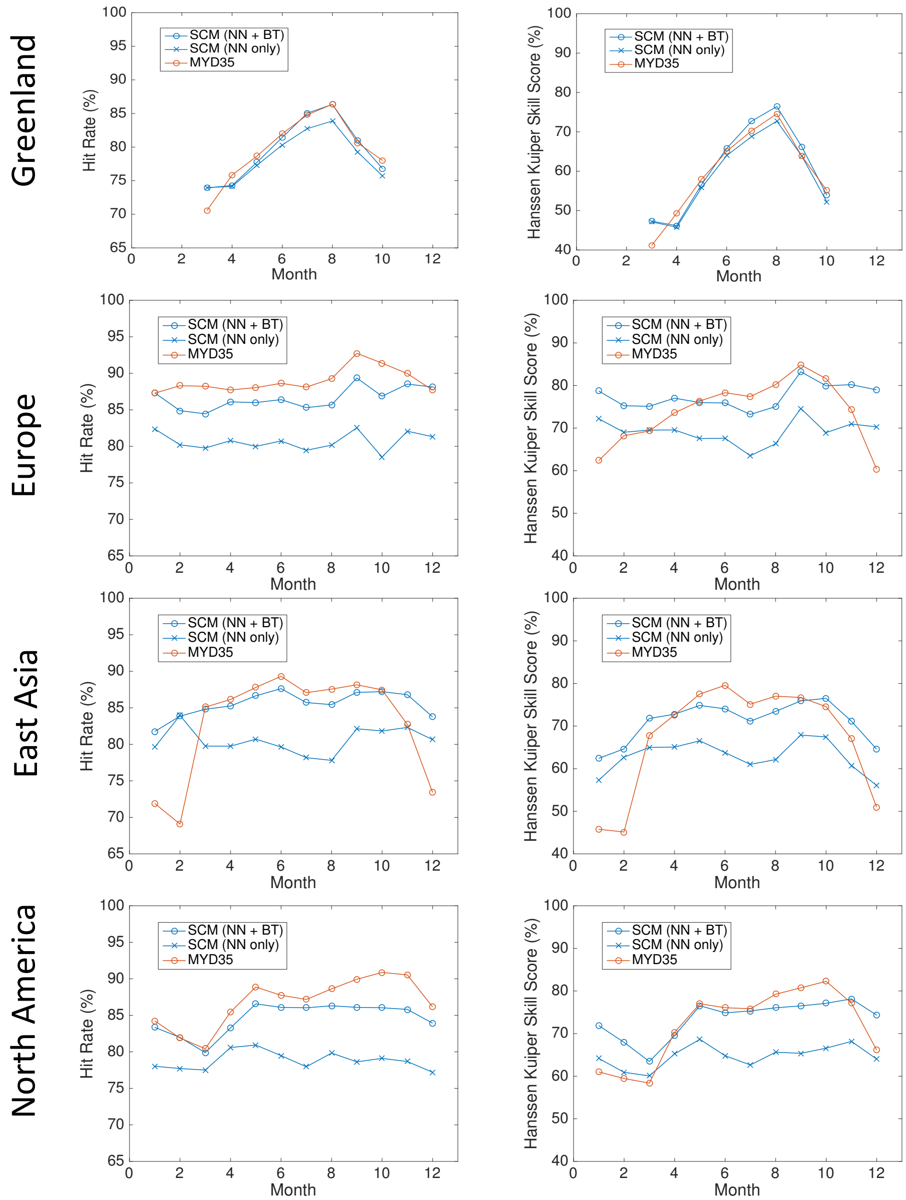

Figure 6: Hit rate (left) and Hanssen Kuiper Skill Score (right) of our cloud mask algorithm (SCM) and MYD35 in 2008 over Greenland, Europe, East Asia, and North America.

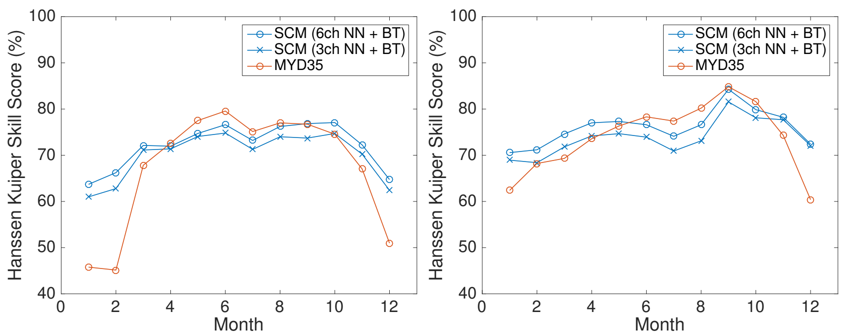

Figure 7: Hanssen Kuiper Skill Score of our cloud mask algorithm (SCM) and MYD35 in 2008 over East Asia (left) and Europe (right). Note the superior performance of the SCM in the winter season.

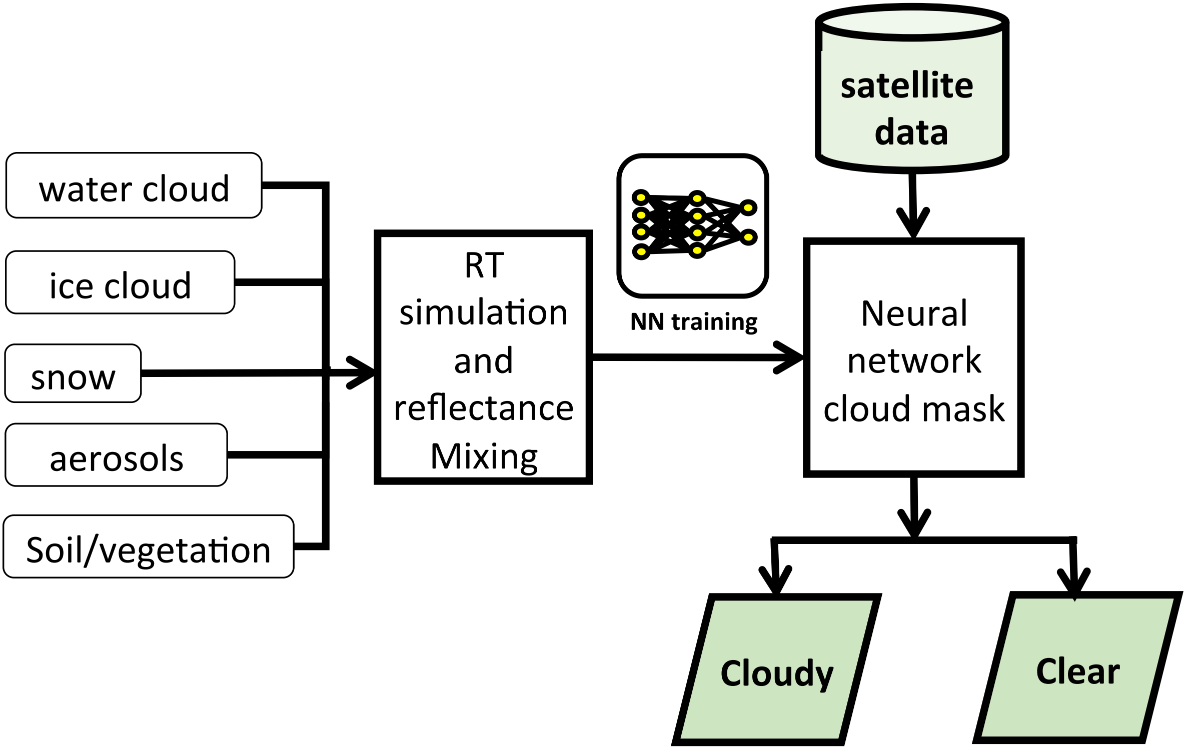

satellite data
water cloud
ice cloud
snow
aerosols
Soil/vegetation
RT simulation and reflectance Mixing
NN training
Neural network cloud mask
Cloudy
Clear

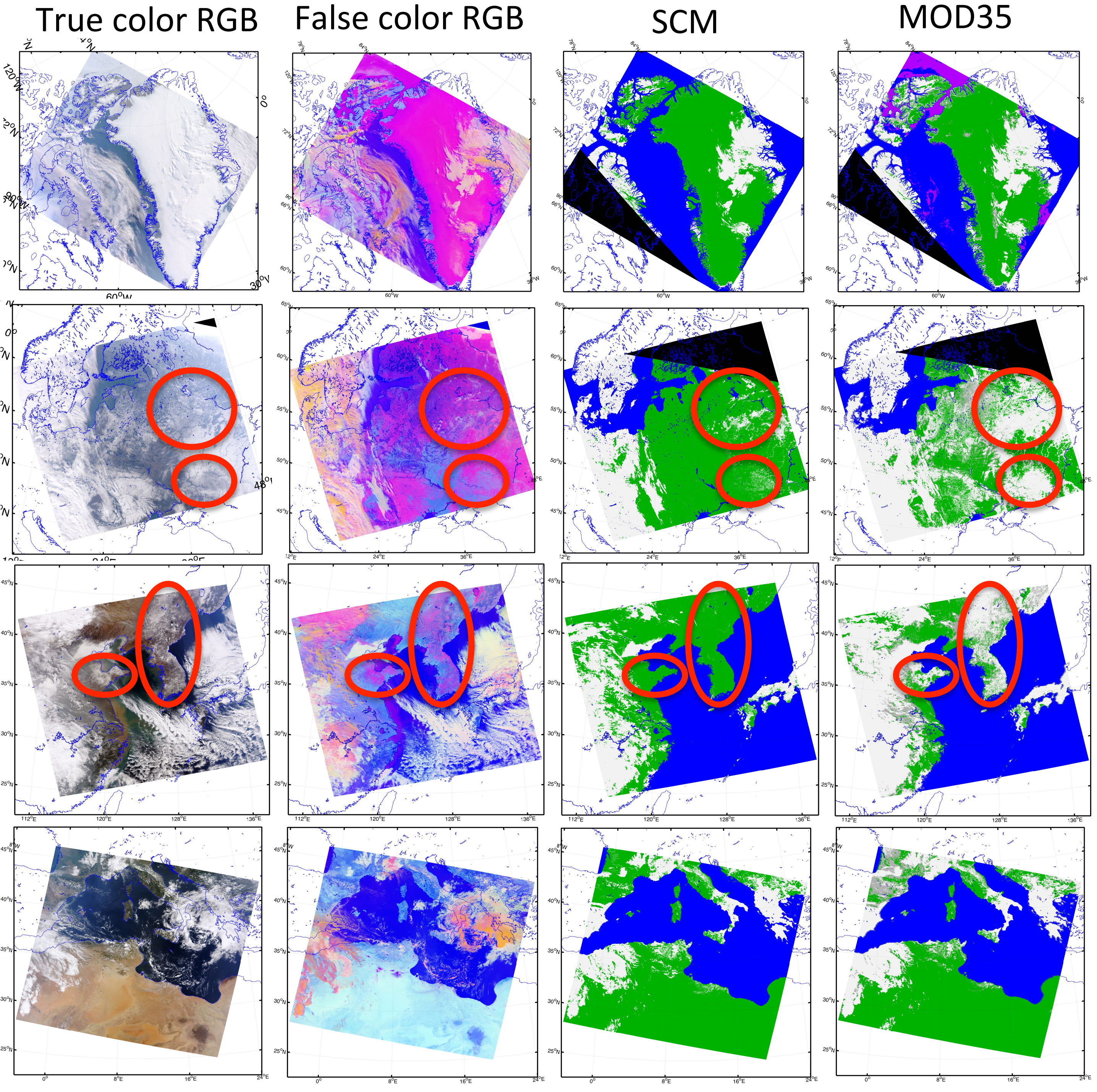
True color RGB
False color RGB
SCM
MOD35

Figure_val_area

Click here to download high resolution image

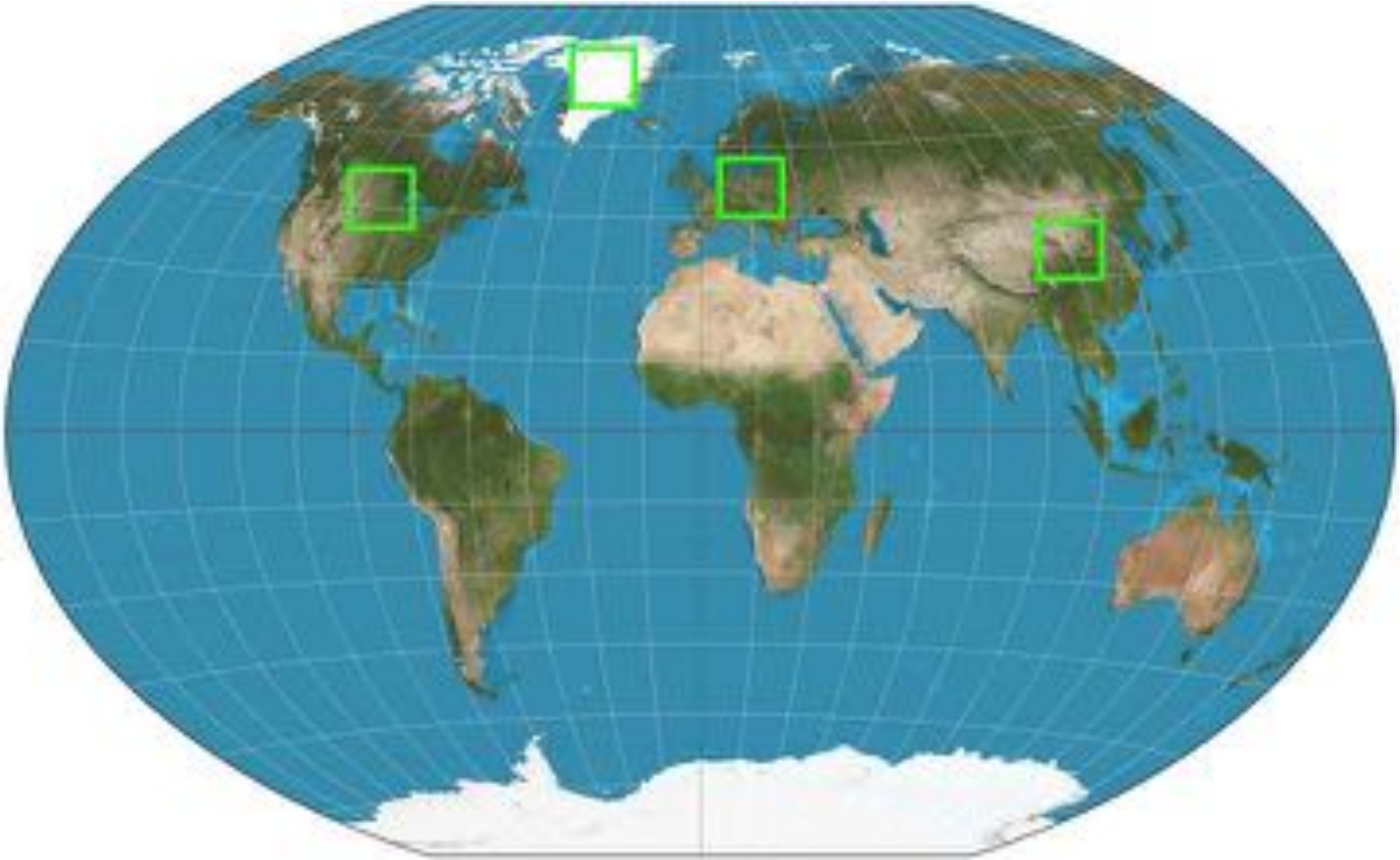

Figure_3ch_asia
Click here to download Figure: TSS_SCM_vsCALIOP_monthly_East_Asia_2008_3ch_6ch.pdf

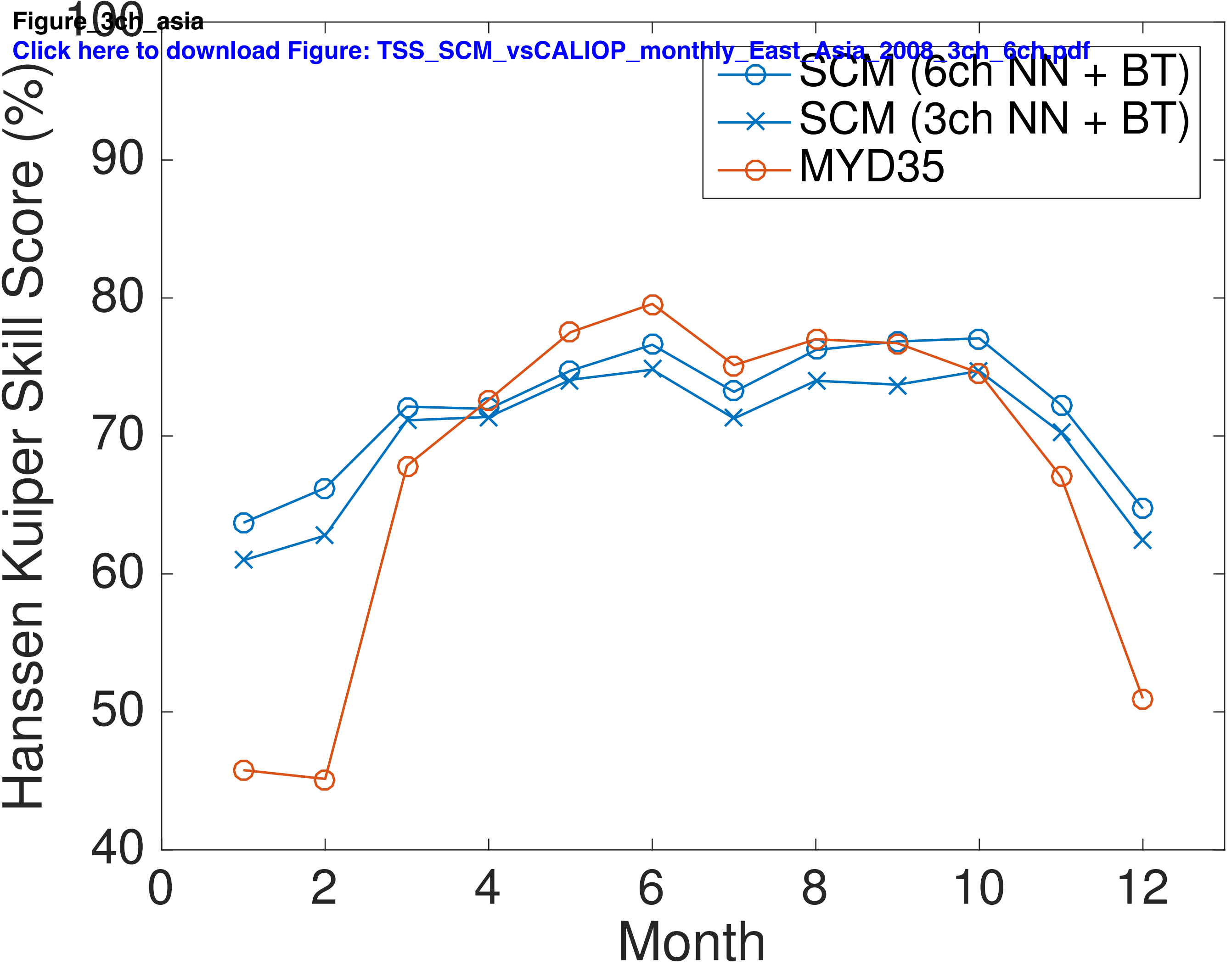

Figure_3ch_europe

Click here to download Figure: TSS_SCM_vsCALIOP_monthly_Europe_2008_3ch_6ch.pdf

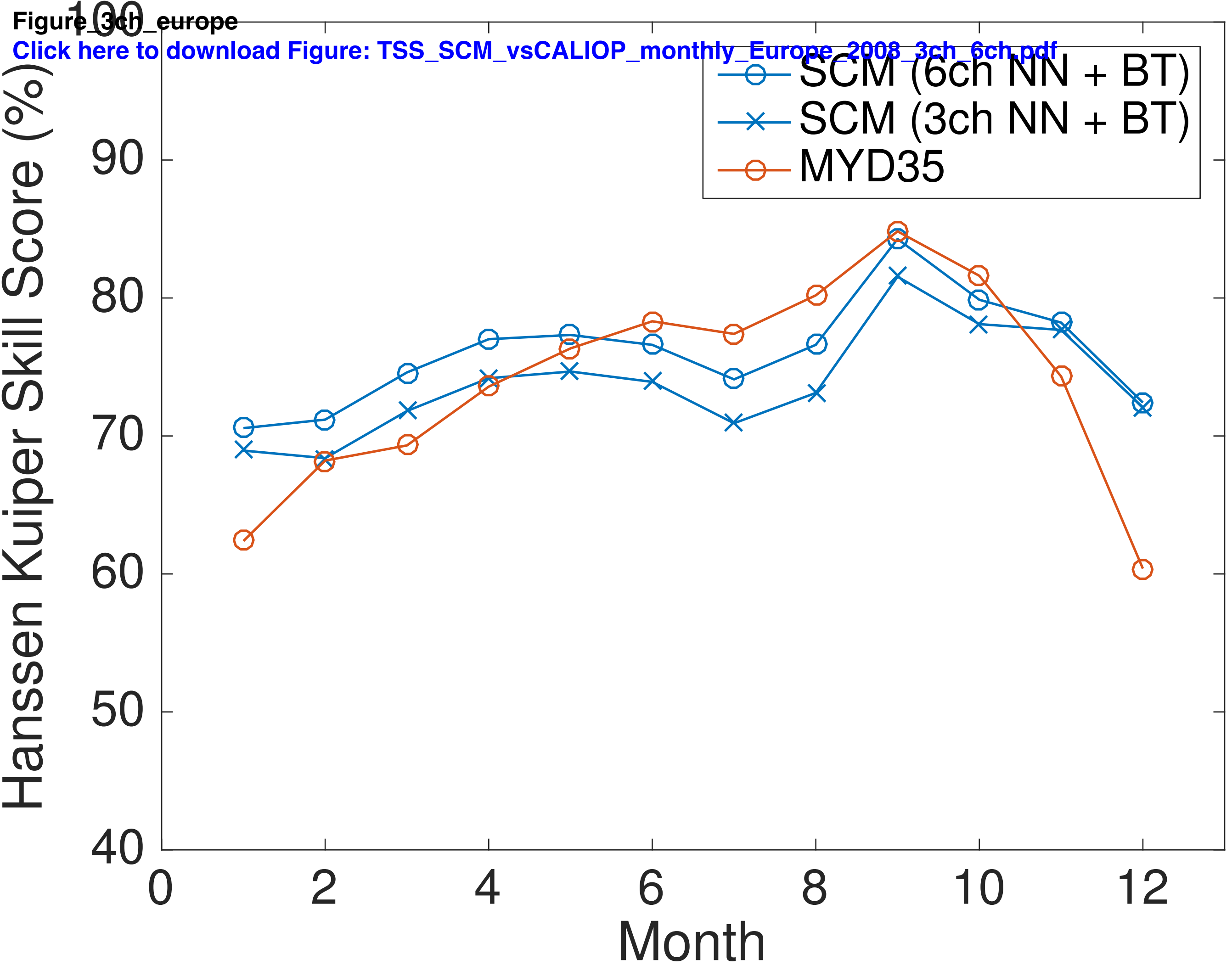

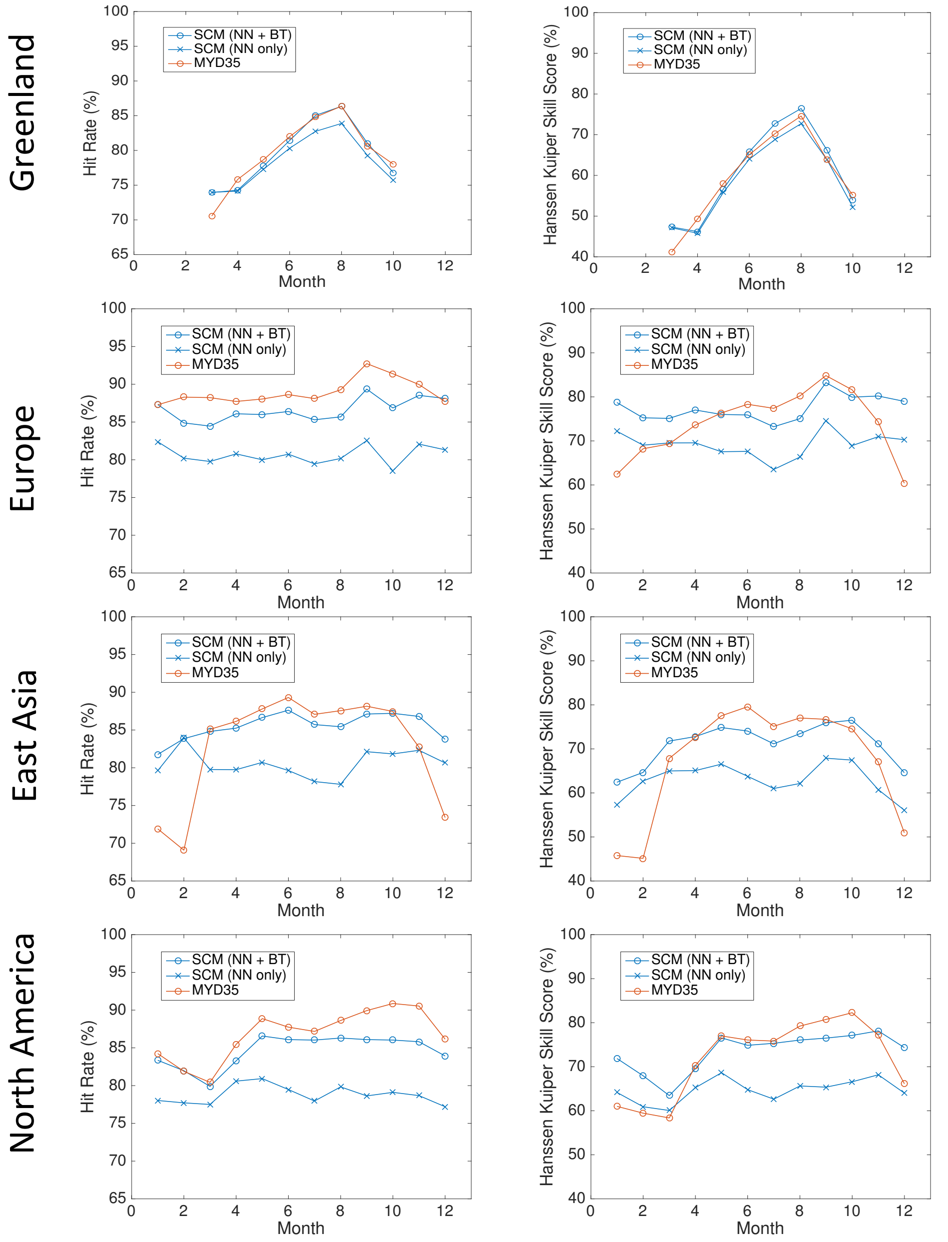
Greenland
Europe
East Asia
North America
SCM (NN + BT)
SCM (NN only)
MYD35
Hit Rate (%)
Hanssen Kuiper Skill Score (%)
Month

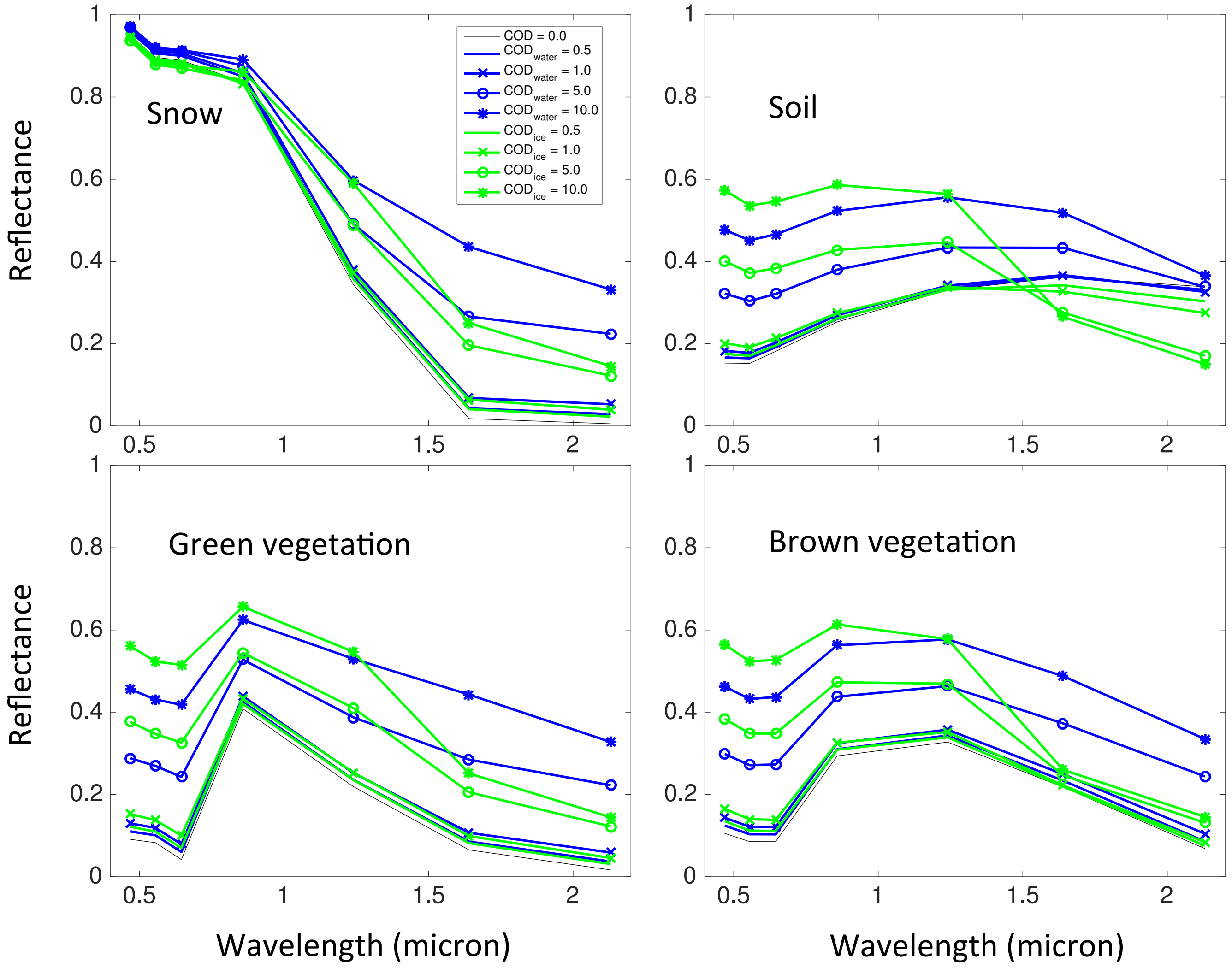

Snow
Soil
Green vegetation
Brown vegetation
Reflectance
Wavelength (micron)
COD = 0.0
COD water = 0.5
COD water = 1.0
COD water = 5.0
COD water = 10.0
COD ice = 0.5
COD ice = 1.0
COD ice = 5.0
COD ice = 10.0

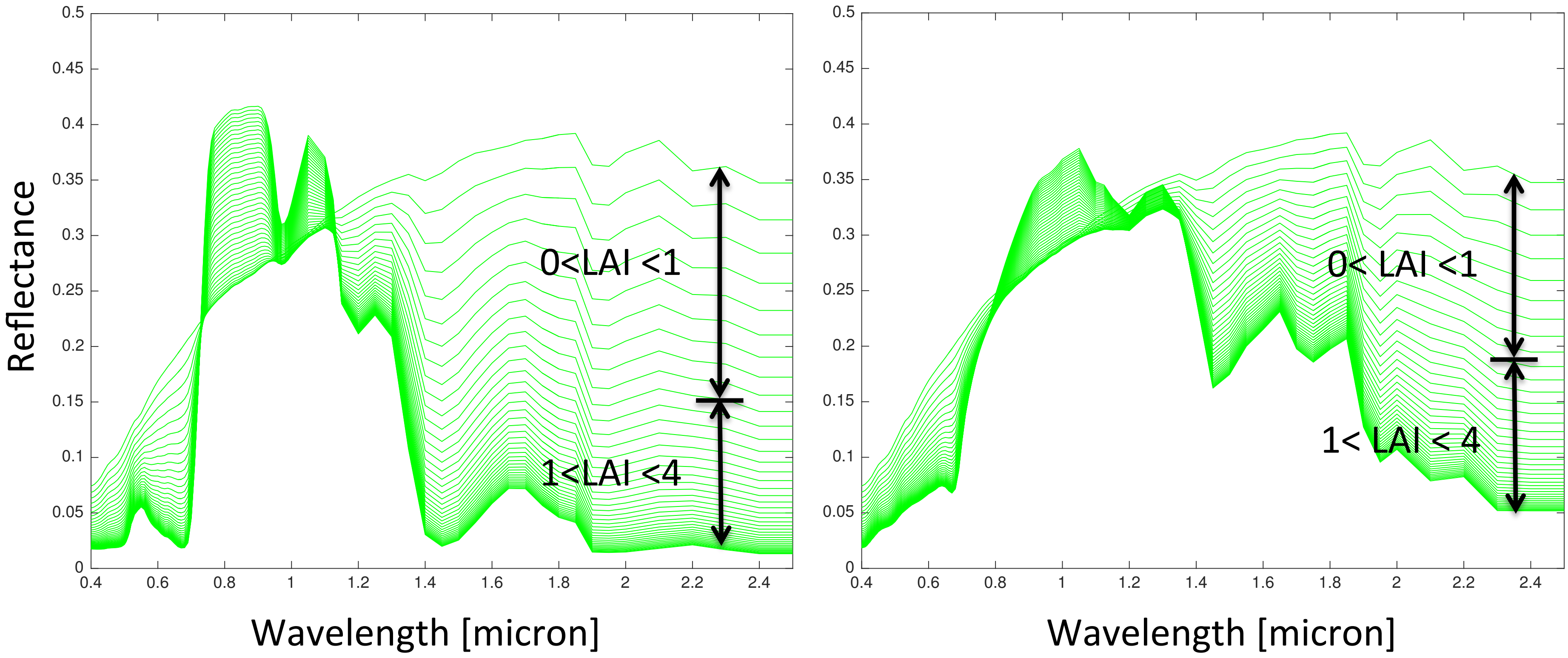
Reflectance
0.5
0.45
0.4
0.35
0.3
0.25
0.2
0.15
0.1
0.05
0
0.4
0.6
0.8
1
1.2
1.4
1.6
1.8
2
2.2
2.4
0<LAI <1
1<LAI <4
Wavelength [micron]
0< LAI <1
1< LAI < 4
Wavelength [micron]